Cyclical MinD membrane affinity differences are not necessary for MinD gradient formation in *Bacillus subtilis*

Laura C. Bohorquez[1, 4], Henrik Strahl[2, #], Davide Marenduzzo[3], Martin J. Thiele[2, 5], Frank Bürmann[2, 6], Leendert W. Hamoen[1, #]

[1] The Bacterial Cell Biology, Swammerdam Institute for Life Sciences, University of Amsterdam, Amsterdam, The Netherlands.

[2] The Centre for Bacterial Cell Biology, Biosciences Institute, Newcastle University, Newcastle upon Tyne, United Kingdom.

[3] SUPA, School of Physics and Astronomy, The University of Edinburgh, Edinburgh, Scotland, United Kingdom.

[#] For correspondence: Henrik Strahl (h.strahl@ncl.ac.uk), Leendert Hamoen (l.w.hamoen@uva.nl)

[4] Present address: FIND, Geneva, Switzerland

[5] Present address: Carl Zeiss Meditec AG, Jena, Germany

[6] Present address: MRC Laboratory of Molecular Biology, Structural Studies Division, Cambridge, UK

Running title: Effect of MinD membrane affinity on gradient formation

ABSTRACT

Proteins can diffuse micrometers in seconds, yet bacterial cells are able to maintain stable protein gradients. The best studied bacterial protein gradient is the Min system of *Escherichia coli*. In rod-shaped bacteria the MinCD proteins prevent formation of minicells by inhibiting FtsZ polymerization close to the cell poles. In *E. coli* these proteins oscillate between cell poles within a minute, resulting in an increased MinCD concentration at the poles. This oscillation is caused by the interaction between MinD and the protein MinE, which form an ATP-driven reaction-diffusion system, whereby the ATPase MinD cycles between a monomeric cytosolic and a dimeric membrane attached states. *Bacillus subtilis* also has MinCD, but lacks MinE. In this case MinCD form a static gradient that requires the transmembrane protein MinJ, located at cell poles and cell division sites. A recent reaction-diffusion model was successful in recreating the MinD gradient in *B. subtilis*, assuming that MinD cycles between cytosol and membrane, like in *E. coli*. Here we show that the monomeric and dimeric states of *B. subtilis* MinD have comparable membrane affinities, that MinD interacts with MinJ as a dimer, and that MinJ is not required for membrane localization of MinD. Based on these new findings we tested different models, using kinetic Monte Carlo simulations, and found that a difference in diffusion rate between the monomer and dimer, rather than a difference in membrane affinity, is important for *B. subtilis* MinCD gradient formation.

42 **IMPORTANCE (150 max)**

43

44 Proteins can diffuse micrometers in seconds, yet bacterial cells are able to maintain stable
45 protein gradients. One of the best studied examples is the membrane associated MinD
46 protein gradient in *Escherichia coli*. This oscillating gradient requires cycling of MinD
47 between a monomeric cytosolic and a dimeric membrane attached state. *Bacillus subtilis*
48 also has a Min system, but in this case MinD forms a static gradient. Mathematical models
49 have been successful in recreating the MinD gradient in *B. subtilis*, using an *E. coli*-like
50 membrane attachment cycle of MinD. Here we show that, in contrast to the *E. coli* situation,
51 the monomeric and dimeric state of *B. subtilis* MinD have comparable membrane affinities.
52 Using this and other information, we tested Monte Carlo simulations and found that a
53 difference in diffusion rate between MinD monomer and dimer, rather than a difference in
54 membrane affinity, is important for MinD gradient formation in *B. subtilis*.

55 **INTRODUCTION**

56

57 Bacterial cells are capable of positioning proteins at midcell and cell poles, and can form
58 protein gradients without the support of specific membrane compartments or guidance by
59 cytoskeleton elements, as found in eukaryotic cells. A well-known example is the formation
60 of a MinCD protein gradient along the cell axis of rod-shaped *E. coli* and *B. subtilis* cells. The
61 formation of these protein gradients is remarkable considering that the diffusion of proteins
62 in cells is in the order of µm square per second, whereas these bacteria are only a few µm in
63 length (1).

64 The Min system of *E. coli* is the best studied gradient system, and comprises the
65 membrane associated MinD and MinE proteins that form a reaction-diffusion couple
66 resulting in a MinCD gradient that oscillates between cell poles in a matter of seconds (2, 3).
67 This system has been reconstructed on artificial membranes resulting in dynamic wave
68 patterns (4), and extensively simulated to understand the reaction parameters (e.g. (5-11)).
69 *B. subtilis* also forms a MinD gradient that decreases in concentration from cell poles and
70 nascent cell division sites towards the middle of the cell. However, unlike *E. coli*, this
71 gradient does not oscillate (12-14). In this study, we investigated how the MinCD gradient is
72 formed in *B. subtilis*.

73 The core of the Min system consists of the protein couple MinC and MinD that
74 prevent aberrant polymerization of the key cell division protein FtsZ close to newly formed
75 septa or cell poles (14-16). MinC inhibits polymerization of FtsZ by direct protein-protein
76 interactions and needs to bind to the Walker A-type ATPase MinD for its activity (17-20). In
77 case of *E. coli* MinD, ATP binding leads to dimerization of MinD, which induces a
78 conformational change in the C-terminal region, thereby exposing an amphipathic helix that

79 functions as a membrane binding domain (18, 21). The MinD dimer recruits MinC to the cell
80 membrane and stimulates its activity (21-23). The *E. coli* Min system comprises a third
81 protein, the peripheral membrane protein MinE, that interacts with MinD, thereby
82 displacing MinC and stimulating the ATPase activity of MinD, which ultimately triggers the
83 release of MinD from the membrane (22, 24-27). The interaction with MinD causes a
84 conformational change in MinE that stimulates its membrane affinity (24). These reciprocal
85 interactions of MinD and MinE represent a natural reaction-diffusion system, resulting in
86 the oscillation of MinCD proteins between cell poles with a periodicity of approximately 50
87 seconds (2-4). Through this oscillation, the average concentration of MinC is higher close to
88 cell poles and lower at midcell, thereby inhibiting polymerization of FtsZ close to cell poles
89 and favoring Z-ring formation at midcell (28).

90 The MinCD proteins of *E. coli* and *B. subtilis* are highly conserved. However, *B.*
91 *subtilis* does not encode a MinE homologue and instead requires the proteins DivIVA and
92 MinJ for the proper polar and septal localization of MinCD (29, 30). DivIVA is a general
93 scaffold protein conserved in Gram-positive bacteria that associates with strong negatively
94 curved membrane areas at the base of division septa, resulting in polarly located DivIVA
95 clusters after division is completed (31, 32). The integral membrane protein MinJ interacts
96 with DivIVA and shows the same localization pattern. MinJ also interacts with MinD, and
97 inactivation of MinJ eliminates a MinCD gradient, resulting in filamentous cells and minicell
98 formation due to uncontrolled activity of MinC (29, 30). Since DivIVA is recruited to midcell
99 in the early stages of septum synthesis when a strong concave membrane area is formed
100 (31), the Min proteins are already present when septum synthesis is ongoing, and their
101 primary activity it to inhibit Z-ring formation next to nascent division sites (14).

102 The ATP-driven cycle between membrane association and dissociation of MinD is

critical to the formation of the oscillating MinD gradient in *E. coli*. Mathematical modelling has shown that such an ATP-driven reversible membrane attachment cycle can also explain the formation of a MinD gradient in *B. subtilis* (33, 34). However, the C-terminal amphipathic alpha helix of *B. subtilis* MinD has a much stronger affinity for the cell membrane compared to its *E. coli* counterpart, and when fused to GFP can recruit this protein to the cell membrane, which the *E. coli* MinD C-terminal membrane anchor is not capable of (35). In fact, a MinD point mutant that prevents binding of ATP and maintains the protein in its monomeric state is still recruited to the *B. subtilis* cell membrane (36). It is therefore unclear whether dimerization-dependent changes in the membrane affinity of the MinD are crucial for the formation of a *B. subtilis* MinCD gradient.

In this study, we analyzed and manipulated the membrane affinity of *B. subtilis* MinD, and combined *in vivo* experiments with *in silico* Monte Carlo simulations to assess the role of membrane affinity in the formation of a MinCD gradient. These experiments demonstrate that, unlike in *E. coli*, a difference in membrane affinity between MinD monomer and dimer is not critical for the creation of a MinCD gradient. In addition, we examined how differences in MinD membrane affinity affect the recruitment of MinC to the membrane, a process that is critical for the FtsZ-regulating activity of the Min-system.

120 **RESULTS**

121

122 **Effect of dimerization on the localization of *B. subtilis* MinD**

123 We began by examining how much the membrane affinity of monomeric *B. subtilis* MinD
124 differs from the dimeric form by constructing MinD variants that are fixed in one of these
125 conformations. Dimerization of MinD and other members of the MinD/ParA protein family
126 requires binding of ATP. The conserved lysine in the Walker A-type ATPase domain, amino
127 acid position 16 in the protein (Fig. S1), forms hydrogen bonds with the phosphate groups of
128 the nucleotide, as revealed in the crystal structure of *Pyrococcus furiosus* MinD (37).
129 Exchanging this residue into an alanine (K16A exchange) prevents ATP binding and
130 formation of dimers in several Walker motif-containing proteins, including *E. coli* MinD and
131 RecA, and *B. subtilis* ParA/Soj (26, 38-40). The conserved glycine at position 12 makes
132 contacts with the γ-phosphate of ATP across the dimer interface. It has been shown that
133 changing this residue into a valine in *B. subtilis* ParA and *E. coli* MinD causes a steric clash in
134 the active site, thereby preventing dimerization while retaining ATP binding (38, 40). These
135 two monomer-forcing amino acid exchanges (K16A and G12V) were introduced into *B.*
136 *subtilis* MinD, which was fused at the N-terminus with GFP to follow its localization in the
137 cell. It has been shown that a GFP-MinD fusion retains its biological activity (13), and the
138 fusion protein was expressed at levels that resulted in normal sized cells and the absence of
139 minicells (Fig. 1A). To prevent possible localization artefacts due to the weak dimerization
140 characteristics of GFP (41), we used a monomeric GFP (mGFP) variant. The different MinD
141 fusion proteins were expressed from the ectopic *amyE* locus, under control of the xylose-
142 inducible *Pxyl* promoter (42), in a strain lacking wild type *minD* (Δ*minD*), as well as in a strain
143 lacking *minD* and *minC* (Δ*minCD*). Western blot analysis showed that the different MinD-

144 variants were stable and expressed at levels comparable to that of wild type MinD (Fig. S2).
145 Induction of mGFP-MinD with 0.1 % xylose reduced minicell formation in a Δ*minD*
146 background to wild type levels (from 14.7 % to 0.07 %, n > 300). However, the mGFP-MinD-
147 K16A and -G12V variants were unable to prevent formation of minicells (11.2 % and 9.5 %,
148 respectively, n > 600).

149 Fig. 1B shows the effect of the K16A exchange on mGFP-MinD localization. In line
150 with previous results (36), preventing the binding of ATP abolishes the mGFP-MinD
151 concentration gradient, which becomes clearer in longitudinal fluorescence intensity
152 profiles (Fig. 1, right panels). The fluorescence peaks visible at midcell are caused by the
153 presence of two septal cell membranes layers, as indicated by the fluorescence intensity
154 profiles of a wild type cell stained with the fluorescent membrane dye FM 5-95 (Fig. 1G).

155 The monomeric ATP binding G12V variant shows the same absence of a protein
156 gradient as the K16A variant (Fig. 1C). In contrast to *E. coli* MinD (26), both monomeric *B.*
157 *subtilis* MinD mutants still bind to the cell membrane. To measure the membrane
158 association *in vivo*, transverse fluorescence intensity profiles were collected (Fig. 1, middle
159 panels), and the membrane affinities were estimated based on the ratio between valley
160 (cytoplasmic) and peak (membrane) signals. This confirmed that the different monomeric
161 mutants have the same membrane affinity as wild type MinD (Fig. 1F). As controls we used
162 the fluorescence membrane dye FM5-95 and cells expressing cytosolic GFP (Fig. 1E).

163 It has been shown that exchanging a conserved aspartic acid residue in the ATPase
164 domains of *B. subtilis* ParA and *E. coli* MinD blocks ATP hydrolysis and traps the proteins in a
165 dimeric state (38, 40). When this aspartic acid residue, located at amino acid position 40 in
166 the *B. subtilis* MinD sequence (Fig. S1), was replaced by an alanine in the mGFP-MinD fusion,
167 expression of this variant in a Δ*minD* strain resulted in highly filamentous cells with clusters

168 of mGFP-MinD-D40A formed along the membrane (Fig. 1D, left picture). Introduction of a
169 *minC* deletion restored cell division (Fig. 1D, right picture), indicating that the locked MinD
170 dimer causes hyper activation of MinC. Interestingly, in this Δ*minCD* background the clusters
171 disappeared and mGFP-MinD-D40A showed a clear polar and septal accumulation, although
172 the polar and septal signal intensities were approximately 60-70 % compared to that of wild
173 type cells (Fig. S3B), and the longitudinal protein gradient was clearly reduced (Fig. 1D).
174 Quantification of the membrane affinity showed that the membrane affinity of the D40A
175 variant is only slightly higher compared to the monomeric mutants (Fig. 1F).
176

177 **Localization of trapped MinD dimer depends on MinJ**

178 The polar and septal localization of the D40A trapped dimer-variant of MinD presumably
179 relies on the interaction with MinJ. It has been reported that the absence of MinJ results in
180 detachment of MinD from the membrane (29, 34). However, when we introduced the Δ*minJ*
181 in our Δ*minCD* deletion strain background we found that all MinD-GFP variants remained
182 attached to the membrane (Fig. S4), and the septal and polar localization of wild type and
183 the trapped dimer MinD disappeared. These results show that while MinJ is not required for
184 membrane attachment of MinD *per se,* it is required for polar and septal localization of
185 MinD through interactions specifically with the dimeric form of MinD.
186

187 **Recruitment of MinC by the different MinD mutants**

188 Several biochemical studies with different bacterial species, including *B. subtilis*, have shown
189 that MinC and MinD dimers can assemble into long polymers (43-46). However, the
190 assembly of large MinCD multimers has not been observed *in vivo*, and a genetic study
191 indicated that the formation of such polymers are not necessary for the function of the Min

192 system in *E. coli* (47). The D40A MinD variant showed a clustered membrane localization
193 pattern that resolved into a smooth membrane pattern when *minC* was deleted (Fig. 1D).
194 This change in localization pattern might be related to the formation of higher-order MinCD
195 assemblies. To confirm this, we introduced an active mCherry-MinC fusion to see whether
196 mGFP-MinD and mCherry-MinC would colocalize when the former is fixed in a dimeric state.
197 First, we examined the localization of MinC in the presence of monomeric K16A and G12V
198 MinD variants. As shown in Fig. 2B and C, the mCherry-MinC signal was dispersed
199 throughout the cytosol in these strains, indicting a lack of interaction with monomeric MinD
200 variants, in line with a previous report (36). In case of the mGFP-MinD-D40A variant, the
201 mCherry-MinC expression was only induced for 1 h to prevent excessive filamentation. As
202 shown in Fig. 2D, the mCherry-MinC signal showed foci along the membrane that often
203 colocalized with mGFP-MinD-D40A foci, confirming that MinD dimerization is crucial for
204 MinC interaction, and that both proteins can indeed form large assemblies in the cell,
205 presumably in the form of MinCD copolymers.

206 The colocalization of the MinD-D40A and MinC fluorescent fusion proteins enabled
207 us to investigate whether MinD dimerization is sufficient for MinC activity or whether
208 localization at the cell membrane is also required. To test this, the membrane binding
209 capacity of MinD was impaired by replacing isoleucine 260, located in the C-terminal
210 membrane targeting amphipathic alpha helix, with a glutamate residue (Fig. 2E) (48). Next,
211 we introduced this mutation in the mGFP-MinD-D40A mutant to create a trapped MinD
212 dimer that was no longer able to bind to the membrane. Expression of this cytosolic MinD
213 variant did not result in cell filamentation (Fig. 2F), indicating that interaction with MinD
214 dimers alone is not sufficient to inhibit FtsZ polymerization. Rather, MinC needs to be
215 localized and enriched to the membrane surface to be effective, which is not surprising

216 since Z-ring formation occurs at the membrane periphery.

217

218 **Weak membrane interaction is important for MinD gradient formation**

219 The absence of a clear difference in membrane affinity between monomeric and dimeric
220 MinD raised the question whether a reversable membrane binding is important for the
221 formation a protein gradient. To examine this, we tried to increase the membrane affinity of
222 MinD by adding an extra copy of its C-terminal membrane targeting amphipathic helix. The
223 extra amphipathic helix was connected to the original helix by a short 11 amino acid long
224 flexible linker (Fig. 3A). First, we tested whether such tandem amphipathic helix (2xAH)
225 increases the membrane affinity by fusing it to mGFP. As shown in Fig. 3, fusion of this
226 tandem helix to mGFP increased the membrane association of the latter considerably when
227 compared to a single MinD amphipathic helix.

228 Next, we replaced the membrane targeting amphipathic helix of mGFP-MinD by the
229 tandem amphipathic helix. Western blot analysis showed that this new C-terminus did not
230 affect the protein levels to a significant degree (Fig. S2). As shown in Fig. 4B, the tandem
231 helix notably increased the fluorescent membrane signal all along the cell membrane (Fig.
232 4D and S5), thereby reducing the longitudinal fluorescence gradients.

233 To confirm that the tandem amphipathic helix increased the membrane affinity of
234 MinD, we tested its sensitivity to membrane depolarization. Previously, it has been shown
235 that binding of the MinD amphipathic helix to the cell membrane requires the presence of
236 the membrane potential (48). Dissipation of the proton motive force by the specific proton-
237 ionophore carbonyl cyanide m-chlorophenylhydrazone (CCCP) did not affect the membrane
238 localization of the tandem amphipathic helix fusion, whereas CCCP quickly disturbed the
239 membrane attachment of wild type MinD (Fig. S6).

240 We also tested what happens with the MinD gradient when its membrane affinity is
241 reduced. For this, the well-studied membrane binding amphipathic helix 2 from the
242 Hepatitis C virus protein NS4B was chosen (49, 50), which is hardly able to attach mGFP to
243 the cell membrane (Fig. 3). Replacing the wild type membrane targeting helix of MinD by
244 the weak NS4B amphipathic helix reduced the membrane association of mGFP-MinD (Fig.
245 4D), as well as its septal and polar localization (Fig. 4C and Fig. S5). Interestingly, this mutant
246 still displayed a longitudinal protein gradient. Together these data suggests that a reversible
247 membrane association is important for the formation of a MinD gradient along the cell axis.
248

249 **Effect of MinD membrane affinity on MinC recruitment and activity**

250 The results shown in Fig. 2 indicated that the attachment of the MinD dimer to the
251 membrane is essential for the activity of MinC. When this attachment was strengthened by
252 using the tandem amphipathic helix, the respective strain regularly featured additional
253 septa resulting in minicells (Fig. 4B, red arrows), although the frequency was lower
254 compared to a Δ*minD* mutant (Fig. 5A). The strain also exhibited an elongated cell
255 phenotype that was comparable to that of the *minD* deletion strain (Fig. 5B). As shown in
256 Fig. 6A-B, the mGFP-MinD(2xAH) variant is capable of recruiting mCherry-MinC along the
257 whole cell membrane, which likely explains the elongated cell phenotype.

258 Weakening the membrane affinity of mGFP-MinD, by replacing the wild type
259 amphipathic helix with the NS4B amphipathic helix, also resulted in occasional minicell
260 formation, but again not as numerous as in a *minD* deletion strain (Fig. 5A). The cell length
261 distribution of the strain expressing the mGFP-MinD(NS4B-AH) variant was closer the wild
262 type strain (Fig. 5B). When mCherry-MinC was co-expressed in this strain background, also
263 the MinC fusion protein showed a clear fluorescent gradient along the cell axis (Fig. 6C).

264 Thus, a reversible association of MinD with the cell membrane seems to be critical to
265 prevent misplacing the FtsZ inhibiting activity of MinC along the cell axis. Both the mGFP-
266 MinD(2xAH) and mGFP-MinD(NS4B-AH) variants were, at least partially, able to prevent
267 minicell formation, presumably because they are still recruited to cell poles and cell division
268 sites through interaction with MinJ.
269

270 **Membrane gradient formation in kinetic Monte Carlo simulations**

271 The different experiments indicated that the formation of a MinCD gradient requires the
272 dynamic switching between monomer and dimer states of MinD (Fig. 1), and a reversible
273 MinD membrane interaction (Fig. 4). So far, *in silico* simulations of the *B. subtilis* Min
274 gradient have assumed a strong difference in membrane interaction between the
275 monomeric and dimeric state of MinD, which is based on properties of the *E. coli* Min
276 system (33, 34). However, our data suggests that for *B. subtilis* these affinities do not differ
277 much (Fig. 1). To investigate more closely whether a difference in membrane affinity
278 between monomer and dimer is required for the formation of a MinD gradient in *B. subtilis*,
279 we resorted to kinetic Monte-Carlo simulations. The Monte-Carlo algorithm attempts to
280 move one molecule at a time by a small amount in a three-dimensional space. The new
281 interaction energy experienced by the particle is then calculated and compared with its old
282 energy, and the move is subsequently accepted or rejected according to the standard
283 Metropolis test (51, 52). This procedure is used to guide the system to the correct
284 Boltzmann distribution in equilibrium. It has been shown that this Monte-Carlo dynamics
285 corresponds well with Brownian or molecular dynamics (53, 54), and can be used to
286 examine mechanisms underlying spatiotemporal protein gradients in cells, provided that the
287 moves are small enough and that the acceptance probability remains high (31).

288 MinD monomers were presented as spheres (hydrodynamic radius 2.5 nm) that
289 diffuse within and along a spherocylindrical cell geometry. The following rules were
290 implemented: (i) Diffusion along the membrane is 10-fold slower that through the
291 cytoplasm, and (ii) the dimer, due to its larger diameter, diffuses 2-fold slower compared to
292 the monomer in both environments, emanating from Stokes-Einstein law and a
293 hydrodynamic radius for the dimer which is double that of the monomer. (iii) Based on the
294 data from Fig. 2, we started out with a 10 % stronger membrane affinity for the dimer. (iv)
295 The membrane dwell time of monomers and dimers is 0.01 - 0.5 sec and during the
296 simulations approximately 70 % of MinD molecules reside at the membrane, approaching
297 the valley to peak values observed experimentally (Fig. 1F). (v) Dimerization and
298 monomerization are modelled as chemical reactions between a monomer and a dimer
299 state. Baseline rates are set such that the two states are in a 1:1 ratio, based on the
300 longitudinal fluorescence intensity profile in Fig. 2A, and the assumption that dimers are
301 located at the polar regions and monomers along the lateral wall. In our baseline model,
302 dimerization at the pole, membrane and in the cytoplasm is equally likely, and is modelled
303 in a simple way as a reaction turning a monomeric to a dimeric MinD at constant rate. (vi)
304 The transition from dimer to monomer, stimulated by ATP hydrolysis, occurs stochastically
305 with a half-life of approximately 1/sec, which is based on information from *E. coli* MinD (8).
306 (vii) MinD dimers that come in close proximity of MinJ, represented as the surface area at
307 the polar caps, will remain attached to MinJ for some time, so that approximately 25 % of
308 MinD dimers is associated with MinJ, reminiscent of the septal localization of the D40A
309 variant (Fig. S3). Simulation details are described in the material and methods.

310 When we applied these rules and ran the simulation, a strong accumulation of MinD
311 at the poles was observed, but no gradient (Fig. 7A). In this simulation, the chance that

312 MinD can form a dimer is the same for monomers in the cytoplasm and those that are
313 attached to the membrane. However, it is likely that dimer formation in the latter situation
314 is more likely since monomers attached to the membrane by their C-terminal amphipathic
315 helix will diffuse slower and therefore spend more time in close proximity and, importantly,
316 they have the same spatial orientation, which will facilitate dimerization. However, when we
317 repeated the simulation, and implemented that membrane attached monomers have a 2-
318 fold higher chance of forming dimers than monomers in the cytoplasm, the localization
319 pattern did not change (Fig. 7B).

320 Since MinJ interacts with MinD dimers, there is the possibility that MinJ actually
321 stimulates MinD dimerization. Interestingly, when this property was added to the
322 simulation, a clear MinD gradient emerged along the cell length, together with a strong
323 polar localization signal (Fig. 7C), a pattern that is in good agreement with the longitudinal
324 fluorescence intensity profiles observed *in vivo* (Fig. 1A). This pattern did not change when
325 we included the condition that only membrane attached dimers are able to revert to
326 monomers (not shown), as suggested by the stimulated ATPase activity of *E. coli* MinD in the
327 presence of liposomes (27). When we performed the simulation of Fig. 7C but now with the
328 assumption that MinJ only stimulates dimerization and does not bind MinD dimers, a MinD
329 gradient is still formed, although the strong accumulation at the polar caps was abolished
330 (Fig. 7D). Subsequently, we repeated the simulation of Fig. 7C under conditions whereby
331 there was no difference in the diffusion rate of monomer and dimer (Fig. 7E). In this case
332 the MinD gradient was completely lost, showing that the differential diffusion of monomers
333 and dimers is necessary to create a steady-state gradient.

334 Next, we tested the role of the membrane affinity in gradient formation. First, the
335 simulation of Fig. 7C was repeated without a difference between the membrane affinity of

336 the MinD monomer and dimer (Fig. 7F). Interestingly, under these conditions the MinD
337 protein gradient is still being formed. When we repeated the simulation of Fig. 7C and kept
338 the 10 % difference in membrane affinity between MinD monomer and dimer, but made
339 their membrane affinities stronger, the gradient was reduced (Fig. 7G), in good agreement
340 with our *in vivo* observation with a MinD variant containing a tandem membrane anchor
341 (Fig. 4B). Lastly, we tested what happens when the simulation of Fig. 7C was repeated with a
342 weaker membrane affinity of MinD. As shown in Fig. 7H, a clear gradient is formed, again in
343 line with what was found when the membrane targeting amphipathic helix of MinD was
344 replaced with the weaker amphipathic helix 2 from Hepatitis C virus protein NS4B (Fig. 4C).

345 In conclusion, our kinetic Monte Carlo simulations suggests that the formation of a
346 MinD gradient requires: (i) a reversible and not too strong interaction of MinD with the
347 membrane, (ii) a clear difference between the diffusion rates of monomer and dimer, (iii) an
348 ATPase driven dimer-monomer cycle, and (iv) the stimulation of dimerization at the cell
349 poles and division sites. Importantly, a difference in membrane affinity between monomer
350 and dimer is not required.

351 **DISCUSSION**

352

353 **Protein gradients in bacteria**

354 Due to their small size, proteins diffuse rapidly throughout bacterial cells, in a matter of
355 seconds, yet stable protein gradients can be found in a large variety of bacteria. What these
356 systems have in common, including the MinD gradient, is a considerably reduced diffusion
357 rate of the proteins involved, which allows stable protein concentration gradients to form.
358 The viscosity of the cell membrane is roughly 100 times larger compared to the cytoplasm
359 (55, 56), and the Min system uses attachment to the cell membrane to slow down diffusion.
360 Another approach to reduce diffusion is to bind to DNA, which occurs in the ParABS system
361 involved in chromosome segregation in the asymmetric bacterium *Caulobacter crescentus*
362 (57). This system consists of the ParA ATPase, which belongs to the same ATPase family as
363 MinD (58) and ParB that binds to *parS* DNA binding sites. The ParA dimers associate with
364 DNA nonspecifically whereby ParB stimulates ATP hydrolysis of ParA dimers, resulting in the
365 dissociation from DNA. The localized dissociation and subsequent increased diffusion rate
366 results in a ParA concentration gradient away from the *parS* locus (59). The cyanobacterium
367 *Synechococcus elongatus* uses the ParA-like protein McdA to position carboxysomes along
368 the longitudinal axis. In this system, the protein McdB, which interacts with carboxysomes,
369 stimulates McdA ATPase activity and its release from DNA, resulting in an oscillation of
370 McdA over the nucleoid (60). Recently it was described that *Staphylococcus aureus* trigger
371 factor (TF) forms a gradient by interacting with the cell division protein FtsK, resulting in an
372 increased TF concentration towards the septal region (61). How TF reduces its diffusion in *S.*
373 *aureus* cells is still unclear but might be a consequence of the fact that the chaperone
374 directly interacts with ribosomes (62), which diffuse much slower due to their size and

375 association with mRNA and nascent polypeptide chains.

376

377 **Previous MinD gradient modelling studies**

378 As mentioned in the introduction, there are many mathematical models describing the
379 oscillating MinD gradient of *E. coli* but so far only two mathematical models focused on the
380 MinD gradient of *B. subtilis* (33, 34). Both models make use of the reversible interaction of
381 MinD with the cell membrane. The first study, almost 20 years ago, modelled the
382 localization of DivIVA and MinD by a reaction-diffusion system in one spatial dimension (33).
383 At that time neither MinJ nor the localization mechanism of DivIVA were known. In this
384 early study both MinD and DivIVA were assumed to cycle between the membrane and the
385 cytosol, and the membrane attachment of DivIVA would depend on MinD, whereas the
386 membrane attachment of the latter would be stabilized at the cell poles by DivIVA.
387 However, we now know that DivIVA binds to the membrane by itself, and there is no
388 interaction between MinD and DivIVA (31).

389 The ATPase stimulated monomer-dimer cycle of MinD was not included in this early
390 model, but it was used in a recent study that employed a minimal reaction-diffusion system
391 in three-dimensional cellular space (34). In this model *B. subtilis* MinD cycles between the
392 cell membrane and cytosol, whereby the membrane detached MinD is in the ADP-bound
393 state and can only rebind after exchanging ADP for ATP, like in *E. coli*. By assuming that the
394 membrane recruitment rate is higher at the poles and septa due to the presence of MinJ or
395 due to a kinetic increase of diffusional impacts with the membrane due to the curved
396 geometry at poles, a steep MinD gradient could be simulated (34).

397

398 **New data on MinD localization**

399 Here, we have shown that monomeric MinD, both in its ATP-bound and unbound state, has
400 a membrane affinity that is comparable to that of the dimeric form of MinD. This shows a
401 clear difference with the *E. coli* situation, where dimerization of MinD causes a
402 conformational change of the C-terminal region enabling the amphipathic helix to insert into
403 the lipid bilayer (Hu & Lutkenhaus 2003). Apparently, the C-terminal amphipathic helix of *B.*
404 *subtilis* MinD is continuously exposed and capable to bind the membrane, thus increasing
405 affinity only by an additive effect upon dimerization.

406 We have also shown that MinJ is not required for the membrane recruitment of
407 MinD. We have no explanation for the differences between our findings and that of the
408 previous studies in which it has been shown that MinJ is needed for the membrane
409 localization of MinD (29, 34). However, since the membrane-targeting amphipathic alpha
410 helix of *B. subtilis* MinD is by itself sufficient to recruit GFP to the cell membrane, even in *E.*
411 *coli*, which does not contain a MinJ homologue (35, 48), it is difficult to envision how the
412 absence of MinJ would bring MinD to the cytosol.

413 In another study, it has been suggested that the C-terminal amphipathic helix of
414 MinD by itself is sufficient to recruit GFP to cell division sites, even in the absence of either
415 MinJ or DivIVA (63). However, as indicated in Fig. 1, the presence of two perpendicular-
416 observed membranes that are formed during septum synthesis gives a higher fluorescence
417 membrane signal, which might have been mistakenly interpreted as septal localization. In
418 addition, in our hands a GFP fusion with the C-terminal amphipathic helix of *B. subtilis* MinD
419 shows a clear fluorescence membrane stain but no accumulation at division sites (Fig. 3B).

420

421 **Kinetic Monte Carlo model**

422 Our *in vivo* findings warranted a new mathematical model to study the formation of the *B.*

423 *subtilis* MinD gradient. The kinetic Monte Carlo model showed that a membrane
424 attachment-detachment cycle is not required to form a protein gradient, but that a dynamic
425 ATP-driven cycle between monomer and dimer is crucial, coupled to the differences in
426 diffusion rates. We have shown that the MinD dimer associates with MinJ, but this by itself,
427 even when the interaction was reversible, was not enough to create a gradient. We ascribe
428 this to the fact that both monomers and dimers bind to the membrane with small difference
429 in affinities in our model, whereas in (34) the monomer state is not membrane-associated.
430 To establish a gradient in our simulations, we needed to include the requirement that MinJ
431 stimulates and/or stabilizes MinD dimerization, but this MinJ activity remains speculative. It
432 should be stressed that MinJ is not crucial for MinD dimerization, since a *minJ* mutant shows
433 a strong filamentous phenotype that can be suppressed by a *minC* deletion, indicating that
434 MinD dimerization, required for MinC activity, also occurs in the absence of MinJ.

435 Although a difference in membrane affinity between monomer and dimer is not
436 necessary to establish a gradient, the modelling shows that a transient and reversible
437 membrane binding of MinD is necessary. This was also confirmed by the reduced formation
438 of a gradient when the membrane affinity of MinD was increased by using a tandem C-
439 terminal amphipathic helix (Fig. 4). This can be explained by considering the emergent
440 length scale over which the gradient develops. As in reaction-diffusion models for
441 morphogenesis, this length scale is given by the square root of a diffusion coefficient over a
442 reaction rate. Our simulations suggest that a possible formula is given by $l \sim \sqrt{\frac{D_d - D_m}{k_m}}$, with
443 D_d and D_m the dimer and monomer diffusion (the relevant rate is that on the membrane),
444 and k_m the rate of conversion between dimers and monomers. Increasing the interaction
445 with the membrane leads to a decrease in diffusivity, and concomitantly a reduction in the

446 length scale over which the gradient can be observed.

447 In our modelling, MinJ is simply represented by the polar cap area. FRAP studies
448 have shown that the recruitment of MinJ to cell poles and division sites is quite dynamic
449 with a fluorescence recovery rate close to a minute (34). However, the fluorescence
450 recovery rate of MinD is approximate 8-fold higher (34). Because of this large difference in
451 diffusion rates, we have ignored the diffusion of MinJ in our modelling. We do not foresee
452 different results if we were to include MinJ diffusion in our Monte Carlo simulations,
453 provided that in steady state MinJ is on average localized at the poles.

454 Another aspect that we have not included in the simulations is MinD polymerization.
455 It has been shown that purified *E. coli* MinD can form large polymers in the presence of ATP
456 (64), although this was not found for purified *B. subtilis* MinD (46). FRAP experiments with
457 *B. subtilis* shows a fluorescence recover rate of seconds for MinD at division sites,
458 suggesting that if such polymers exist, they are not very stable. Nevertheless, any
459 multimerization of MinD dimer will further increase the diffusion difference between
460 monomer and dimer, thus contributing to the formation of a protein gradient.

461 In conclusion, we have shown here that a dynamic cyclic change in membrane
462 affinity of MinD is not required for the formation of a concentration gradient in the cell.
463 Instead, our modelling suggests that stimulation of MinD-dimerization at cell poles and cell
464 division sites is needed. It will be interesting to see whether future experiments proves this
465 prediction right or wrong.

466 **MATERIAL AND METHODS**

467

468 **Bacterial strains, growth conditions and media**

469 Luria-Bertani (LB) agar was used for the routine selection and maintenance of both *B.*
470 *subtilis* and *E. coli* strains. For *B. subtilis*, cells were grown in LB medium or Spizizen minimal
471 salt medium supplemented with 0.05 % yeast extract (SMMY). SMMY consists of 2 g/l
472 $(NH_4)_2SO_4$, 14 g/l K_2HPO_4, 6 g/l KH_2PO_4, 1 g/l sodium citrate, 2 g/l $MgSO_4$, 5 g/l fructose, 2 g/l
473 tryptophan, 0.2 g/l casamino acids and 2.2 g/l ammonium ferric citrate. All strains were
474 grown at 37 °C. The supplements were added as required: 100 µg/ml ampicillin, 5 µg/ml
475 chloramphenicol, 5 µg/ml kanamycin, 100 µg/ml spectinomycin, 10 µg/ml tetracycline and 1
476 µg/ml erythromycin. The *B. subtilis* strains used are listed in Table S1. The mutant strains
477 kindly provided by other labs were transformed into our laboratory strain to ensure that all
478 strains were isogenic.

479

480 **Strain constructions**

481 Molecular cloning, PCR and transformations were carried out by standard techniques.
482 Plasmids and oligonucleotides used in this study are listed in Table S2 and S3, respectively.
483 The *minC*, *minD*, *minCD* and *minJ* gene deletions were introduced from existing strains listed
484 in Table S1 by standard natural transformation (65). The *aprE*-integration vector containing
485 mCherry under an IPTG-inducible promoter (P*spac*) was constructed as follows. The
486 spectinomycin marker of pAPNC213 (66) was replaced with a chloramphenicol resistance
487 cassette (*cat*) using In-Fusion cloning (Clonetech). For this aim pAPNC123 was PCR-linearized
488 with oligonucleotide pair HS05/HS06 and the *cat* cassette was amplified from pSG2 (67)
489 with oligonucleotide pair HS07/HS08. These PCR products were fused together with In-

490 Fusion cloning, resulting in pAPNC*cat,* this plasmid was verified by sequencing. Next, the
491 mCherry encoding gene was amplified using oligonucleotide pair HS437/HS438 and plasmid
492 template pSS153 (68) as template. SalI and BamHI restriction sites were inserted into the
493 primers. The mCherry PCR product and the pAPNC*cat* were digested with SalI and BamHI
494 and ligated. The resulting plasmid was verified by sequencing and named pHJS112.

495 The IPTG-inducible mCherry-*minC* fusion was constructed as follows. A PCR fragment
496 containing *minC* was amplified with oligonucleotide pair LB1/LB2 and genomic DNA of the
497 wild type strain 168 as template. BamHI and EcoRI restriction sites were inserted into the
498 primers. The PCR product and the *aprE*-integration vector pHJS112 were digested with
499 BamHI and EcoRI restriction enzymes and ligated. The resulting plasmid pLB11 was verified
500 by sequencing and transformed into *B. subtilis* competent cells, resulting in strain LB31. The
501 *aprE* integration was verified by PCR, amplifying the genomic DNA with oligonucleotide pair
502 HS508/HS509 and sequencing.

503 The *amyE*-integration vector pSG1730 containing GFP fused to *minD* under a xylose-
504 inducible promoter (12) was used to exchange the *minD* residue glycine 12 to valine (G12V)
505 and aspartic acid 40 to alanine (D40A), by incorporation of the corresponding mutation
506 using the QuickChange site-directed mutagenesis reaction (Stratagene) and the
507 oligonucleotide pairs HS320/HS321 and HS322/HS323, respectively. The resulting plasmids
508 were verified by sequencing and named pHJS115 and pHJS116, respectively. The plasmid
509 pHJS113 containing GFP fused to *B. subtilis minD* coding sequence with the lysine 16 to
510 alanine (K16A) exchange under a xylose-inducible promoter was reported previously (48).

511 Plasmid pSG1729 (42), containing GFP under a xylose-inducible promoter, was used
512 to generate a construct with GFP fused to the native *minD* membrane targeting amphipathic
513 helix (KGMMAKIKSFFG). This domain was amplified from *B. subtilis* wild type strain 168 with

514 oligonucleotide pair FB136/FB149. EcoRI and BamHI restriction sites were inserted into the
515 primers. The PCR product and the plasmid pSG1729 were digested with EcoRI and BamHI
516 restriction enzymes and ligated. The new plasmid was verified by sequencing and named
517 pHJS117. Plasmid pHJS117 was used to generate a construct with GFP fused to two *minD*
518 amphipathic helices in tandem with a short linker of glycines in between (2xAH). This
519 tandem membrane targeting sequence was created by amplification with oligonucleotides
520 FB138/FB149 and pHJS117 as template. The primer FB138 carries a long overhang that
521 generates an extra MinD membrane targeting amphipathic helix fused to the existing
522 membrane targeting domain (KGMMAKIKSFFGVRS**GG**VLEEQNKGMMAKIKSFFG). EcoRI and
523 BamHI restriction sites were inserted into the primers. The PCR product and the plasmid
524 pSG1729 were digested with *Eco*RI and *Bam*HI restriction enzymes and ligated. The new
525 plasmid was verified by sequencing and named pHJS119.

526 Another construct with GFP fused to the NS4B amphipathic helix 2 from Hepatitis C
527 virus (NS4B-AH) was generated as follows. Plasmid pSG1729 was amplified with
528 oligonucleotides FB141/FB149. The primer FB141 carries a long overhang that generates the
529 NS4B-AH anchor (TVTQLLRRLHQWI). EcoRI and BamHI restriction sites were inserted into
530 the primers. The PCR product and the plasmid pSG1729 were digested with EcoRI and
531 BamHI restriction enzymes and ligated. The new plasmid was verified by sequencing and
532 named pHJS121.

533 We constructed two different *amyE*-integration plasmids with GFP fused to *minD*
534 with different membrane targeting sequences. The native *minD* amphipathic helix was
535 either replaced with two *minD* amphipathic helices in tandem with a short linker of glycines
536 in between (MinD2xAH) or with the Hepatitis C virus NS4B amphipathic helix 2 (MinDNS4B-
537 AH). The *minD* gene was amplified from the *B. subtilis* genome (strain 168) with

538 oligonucleotides pairs FB135/FB138 and FB135/FB141, respectively. BamHI and EcoRI
539 restriction sites were inserted into the primers. The primers FB138 and FB141 carry a long
540 overhang that generates the 2xAH and the NS4B-AH, respectively. The digested PCR
541 fragments were ligated with BamHI/EcoRI-linearized pSG1729, containing GFP under a
542 xylose-inducible promoter. The new plasmids were verified by sequencing and named
543 pHJS123 and pHJS125, respectively.

544 Plasmids pSG1730, pHJS113, pHJS115, pHJS116, pHJS123 and pHJS125 were used as
545 template for the QuickChange site-directed mutagenesis reaction (Stratagene) with
546 oligonucleotide pair HS410/HS411 to introduce the A206K exchange in the GFP coding
547 sequence to reduce protein dimerization (mGFP). The resulting plasmids were verified by
548 sequencing and named pLB21, pLB22, pLB23, pLB24, pLB49 and pLB50 respectively.
549 Plasmids pLB21 and pLB24 were used to further exchange the *minD* isoleucine 260 to
550 glutamic acid (I260E) by QuickChange site-directed mutagenesis reaction (Stratagene) with
551 oligonucleotide pair HS205/HS206. The resulting plasmids were verified by sequencing and
552 named pLB71 and pLB72, respectively. These constructs were integrated at the *amyE* locus
553 in different genetic backgrounds.

554

555 **Western blot analysis**

556 To detect the cellular levels of the different GFP-MinD variants the strains were induced
557 with 0.1 % xylose for three doublings. 2 ml of cultures, with comparable ODs were
558 centrifuged and the cell pellets flash frozen in liquid nitrogen. The pellets were then
559 resuspended in 200 µl of buffer containing 10 mM Tris-Hcl pH 8, 100 mM NaCl and 1 %
560 TritonX-100. The cells were lysed with 100 µg/ml lysozyme during 15 min incubation at
561 room temperature. Cell debris were spun down (20 min Eppendorf centrifuge, 14000 rpm,

562 4°C) and 10 µl of samples were loaded onto a 10 % SDS-PAGE followed by separation by
563 electrophoresis at 150 V for 60 min. The proteins were then transferred to a PVDF
564 membrane (Thermo Scientific) with transfer buffer (14.4 g/l glycine, 3 g/l Tris base and 15 %
565 methanol) using mini-wet electroblotting system (Bio-Rad) at 55 V for 130 min. The
566 transferred membrane was then blocked in blocking buffer (1 % skimmed milk powder in
567 TBST buffer 50 mM Tris, 150 mM NaCl and 0.05 % Tween-20) overnight and rinsed twice for
568 5 min in TBST. The proteins were probed with a 1:2000 dilution of rabbit anti-GFP primary
569 antibody (Invitrogen) in 10 ml TBST incubated 1 h, the membrane was washed 3x in TBST
570 and incubated in a 1:20 000 dilution of secondary antibody goat anti rabbit IR dye (Li-cor
571 Biosciences) in 10 ml TBST during 1 h. The immunoblot was developed by using an Odyssey®
572 imaging system (Li-cor Biosciences).
573
574 **Microscopy**
575 Microscopy was performed on an inverted fluorescence Nikon Eclipse Ti microscope
576 equipped with a CFI Plan Apochromat DM 100x oil objective, an Intensilight HG 130bW lamp
577 and C11440-22CU Hamamatsu ORCA camera. Images were analysed using ImageJ v.1.48d5
578 (National Institutes of Health) software and the plugin ObjectJ (69). To measure the
579 transverse fluorescence intensity profiles (FIP), line-scans perpendicular to the cell axis were
580 marked. The polar gradient areas, marked in red in figures, were manually assigned by
581 means of visual inspection of the fluorescence gradient of the FIPs. The membrane affinity
582 was estimated as the ratio valley/peaks of the transverse FIP, using an average of at least 30
583 cells per data set.
584 For microscopy, cells were grown to exponential phase by diluting 1:100 a starter
585 culture grown overnight in liquid medium (SMMY) into fresh medium, and allowing at least

586 three doublings before mounting on microscopy slides covered with a thin film of 1 %
587 agarose. 0.1 % xylose and 0.01 mM IPTG were used for the induction since these
588 concentrations complemented a Δ*minCD* deletion strain, preventing minicell formation.
589 Membranes were stained with the fluorescent membrane dye FM-95 (0.5 µg/ml final
590 concentration), incubated for 5 min prior to mounting onto microscope slides covered with
591 a thin film of 1 % agarose. Dissipation of the proton motive force (pmf) was carried out by
592 the addition of 100 µM carbonyl cyanide m-chlorophenylhydrazone (CCCP) for 10 min. CCCP
593 was dissolved in DMSO (0.1 % final concentration of DMSO). As control, cells were
594 incubated with 0.1 % DMSO.
595
596 **Kinetic Monte Carlo simulations**
597 To model the formation of a steady state gradient in *B. subtilis* wild-type cells and mutants,
598 kinetic Monte-Carlo simulation were performed. Kinetic Monte Carlo is a stochastic
599 algorithm which is known to be equivalent to molecular dynamics for sufficiently small local
600 moves (53, 54). The system simulated consisted in a collection of 1000 MinD proteins
601 enclosed inside a spherocylinder (aspect ratio 4, sizes 80 by 20 in simulation units)
602 modelling a *B. subtilis* cell. MinD proteins can be in one of two states, either monomeric (M)
603 or dimeric (D). The M and D states have both affinities for the membrane (the surface of the
604 spherocylinder). To model this, we introduce an attractive potential, a square well with
605 range 1 and strength e_M and e_D for the M and D state respectively. Given our experimental
606 results that the dimer is only weakly stickier than the monomer, we ran our simulations with
607 $e_D = 1.1e_M = 1\ k_BT$. Additionally, the D state, but not the M state, may interact with the caps
608 (poles) in the spherocylinders, with an extra interaction again represented by a square well,
609 with range 1 and strength e_C. This interaction simulates binding between dimeric MinD and

610 MinJ. Various cases were considered but results are reported, for simplicity for two cases
611 only: e_C=0 (no additional polar interaction), or e_C = 0.7 e_M. A third parameter which varies
612 between M and D is the diffusion coefficient: for simplicity, unless otherwise stated, we
613 assume this to scale inversely with molecular weight, so that the diffusivity of the dimer, D,
614 is half that of the monomer, M.

615 Key to the formation of the gradient is the fact that the reaction between the M and
616 D states of MinD is not in thermodynamic equilibrium, as it is linked to ATP hydrolysis. In our
617 model, D turns into M, due to ATP hydrolysis, at a constant rate k_{ATP}, in all cases. We
618 consider instead three cases for the dimerization reaction. In our baseline model the
619 conversion of M into D also occurred at the same rate in the cytoplasm, at the membrane
620 and at the pole. We have set this rate such that the M and D state are on average
621 comparable in steady state, as suggested by our experiments. We also considered the case
622 where dimerization at the membrane occurs 2-fold more often at the membrane, and a
623 third case where polar localization (through MinJ interaction) strongly stimulates
624 dimerization, so that the M to D transition occurs at a rate $k_{pole} >> k_{ATP}$ at poles. When
625 considering polar stimulation, dimerization occurs at a rate $k_{ATP}/10$ in the cytosol; otherwise,
626 rates of dimerization and monomerization in the cytoplasm are equal. The diffusion of
627 monomeric MinD in the cytosol was set to 0.0017 in simulation units (corresponding to
628 approximately 1 micron square per second, see below), where the hydrolysis rate k_{ATP} was
629 set to 10^{-5} (corresponding to 1/s). When considering polar stimulation, we set k_{pole} such that
630 dimerization at the pole occurs with unit probability during a timestep (we have verified
631 though that the results are qualitatively similar down to at least a value of k_{pole} equal to 100
632 k_{ATP}). More details on the parameters used in the model are given in the caption of Fig. 7.

633 To simulate the monomer (K16A) and dimer (D40A) mutants, we used another

634 version of the same model, in which all particles were of type M or D respectively, and the
635 rate of interconversion between the two was set to 0.

636 Simulation units may be mapped to physical units by noting that 1 space and time
637 units in simulations can be made to correspond to 0.08 microns and 10 microseconds,
638 respectively.

639 **ACKNOWLEDGEMENTS**

640

641 We would like to thank especially Norbert Vischer for analysis and quantification of
642 fluorescence images and developing ObjectJ plugins, members of the Bacterial Cell Biology
643 group (University of Amsterdam) for insightful discussions, Dirk-Jan Scheffers for critical
644 reading of the manuscript, and Marc Bramkamp for prior communications. This research
645 was funded by EU Marie Curie ITN grants ATP-BCT (020496-2) and AMBER (317338), Marie
646 Curie CIG grant DIVANTI (618452) and STW Vici grant (12128).

647 **REFERENCES**
648

649 1. Kumar M, Mommer MS, Sourjik V. 2010. Mobility of cytoplasmic, membrane, and
650 DNA-binding proteins in *Escherichia coli*. Biophys J 98:552-9.
651 2. Hu Z, Lutkenhaus J. 1999. Topological regulation of cell division in *Escherichia coli*
652 involves rapid pole to pole oscillation of the division inhibitor MinC under the control
653 of MinD and MinE. Mol Microbiol 34:82-90.
654 3. Raskin DM, de Boer PA. 1999. Rapid pole-to-pole oscillation of a protein required for
655 directing division to the middle of *Escherichia coli*. Proc Natl Acad Sci USA 96:4971-6.
656 4. Loose M, Fischer-Friedrich E, Ries J, Kruse K, Schwille P. 2008. Spatial regulators for
657 bacterial cell division self-organize into surface waves in vitro. Science 320:789-92.
658 5. Howard M, Rutenberg AD, de Vet S. 2001. Dynamic compartmentalization of
659 bacteria: accurate division in *E. coli*. Phys Rev Lett 87:278102.
660 6. Meinhardt H, de Boer PA. 2001. Pattern formation in *Escherichia coli*: a model for the
661 pole-to-pole oscillations of Min proteins and the localization of the division site. Proc
662 Natl Acad Sci U S A 98:14202-7.
663 7. Kruse K. 2002. A dynamic model for determining the middle of *Escherichia coli*.
664 Biophys J 82:618-27.
665 8. Huang KC, Meir Y, Wingreen NS. 2003. Dynamic structures in *Escherichia coli*:
666 spontaneous formation of MinE rings and MinD polar zones. Proc Natl Acad Sci U S A
667 100:12724-8.
668 9. Di Ventura B, Sourjik V. 2011. Self-organized partitioning of dynamically localized
669 proteins in bacterial cell division. Mol Syst Biol 7:457.
670 10. Wurthner L, Brauns F, Pawlik G, Halatek J, Kerssemakers J, Dekker C, Frey E. 2022.
671 Bridging scales in a multiscale pattern-forming system. Proc Natl Acad Sci U S A
672 119:e2206888119.
673 11. Glock P, Brauns F, Halatek J, Frey E, Schwille P. 2019. Design of biochemical pattern
674 forming systems from minimal motifs. Elife 8.
675 12. Marston AL, Thomaides HB, Edwards DH, Sharpe ME, Errington J. 1998. Polar
676 localization of the MinD protein of *Bacillus subtilis* and its role in selection of the
677 mid-cell division site. Genes Dev 12:3419-30.
678 13. Marston AL, Errington J. 1999. Selection of the midcell division site in *Bacillus subtilis*
679 through MinD-dependent polar localization and activation of MinC. Mol Microbiol
680 33:84-96.
681 14. Gregory JA, Becker EC, Pogliano K. 2008. *Bacillus subtilis* MinC destabilizes FtsZ-rings
682 at new cell poles and contributes to the timing of cell division. Genes Dev 22:3475-
683 88.
684 15. Levin PA, Shim JJ, Grossman AD. 1998. Effect of minCD on FtsZ ring position and
685 polar septation in *Bacillus subtilis*. J Bacteriol 180:6048-51.
686 16. Bi E, Lutkenhaus J. 1993. Cell division inhibitors SulA and MinCD prevent formation
687 of the FtsZ ring. J Bacteriol 175:1118-25.
688 17. de Boer PA, Crossley RE, Rothfield LI. 1989. A division inhibitor and a topological
689 specificity factor coded for by the minicell locus determine proper placement of the
690 division septum in *E. coli*. Cell 56:641-9.
691 18. de Boer PA, Crossley RE, Hand AR, Rothfield LI. 1991. The MinD protein is a
692 membrane ATPase required for the correct placement of the *Escherichia coli* division
693 site. EMBO J 10:4371-80.

694 19. Hu Z, Lutkenhaus J. 2000. Analysis of MinC reveals two independent domains
695 involved in interaction with MinD and FtsZ. J Bacteriol 182:3965-71.
696 20. Cordell SC, Anderson RE, Lowe J. 2001. Crystal structure of the bacterial cell division
697 inhibitor MinC. EMBO J 20:2454-61.
698 21. Hu Z, Lutkenhaus J. 2003. A conserved sequence at the C-terminus of MinD is
699 required for binding to the membrane and targeting MinC to the septum. Mol
700 Microbiol 47:345-55.
701 22. Hu Z, Saez C, Lutkenhaus J. 2003. Recruitment of MinC, an inhibitor of Z-ring
702 formation, to the membrane in *Escherichia coli*: role of MinD and MinE. J Bacteriol
703 185:196-203.
704 23. de Boer PA, Crossley RE, Rothfield LI. 1992. Roles of MinC and MinD in the site-
705 specific septation block mediated by the MinCDE system of *Escherichia coli*. J
706 Bacteriol 174:63-70.
707 24. Park KT, Villar MT, Artigues A, Lutkenhaus J. 2017. MinE conformational dynamics
708 regulate membrane binding, MinD interaction, and Min oscillation. Proc Natl Acad
709 Sci U S A 114:7497-7504.
710 25. Hu Z, Lutkenhaus J. 2001. Topological regulation of cell division in E. coli.
711 spatiotemporal oscillation of MinD requires stimulation of its ATPase by MinE and
712 phospholipid. Mol Cell 7:1337-43.
713 26. Hu Z, Gogol EP, Lutkenhaus J. 2002. Dynamic assembly of MinD on phospholipid
714 vesicles regulated by ATP and MinE. Proc Natl Acad Sci USA 99:6761-6.
715 27. Lackner LL, Raskin DM, de Boer PA. 2003. ATP-dependent interactions between
716 *Escherichia coli* Min proteins and the phospholipid membrane *in vitro*. J Bacteriol
717 185:735-49.
718 28. Rowlett VW, Margolin W. 2013. The bacterial Min system. Curr Biol 23:R553-6.
719 29. Bramkamp M, Emmins R, Weston L, Donovan C, Daniel RA, Errington J. 2008. A novel
720 component of the division-site selection system of *Bacillus subtilis* and a new mode
721 of action for the division inhibitor MinCD. Mol Microbiol 70:1556-69.
722 30. Patrick JE, Kearns DB. 2008. MinJ (YvjD) is a topological determinant of cell division in
723 *Bacillus subtilis*. Mol Microbiol 70:1166-79.
724 31. Lenarcic R, Halbedel S, Visser L, Shaw M, Wu LJ, Errington J, Marenduzzo D, Hamoen
725 LW. 2009. Localisation of DivIVA by targeting to negatively curved membranes.
726 EMBO J 28:2272-2282.
727 32. Ramamurthi KS, Losick R. 2009. Negative membrane curvature as a cue for
728 subcellular localization of a bacterial protein. Proc Natl Acad Sci USA 106:13541-5.
729 33. Howard M. 2004. A mechanism for polar protein localization in bacteria. J Mol Biol
730 335:655-63.
731 34. Feddersen H, Wurthner L, Frey E, Bramkamp M. 2021. Dynamics of the *Bacillus*
732 *subtilis* Min System. mBio 12.
733 35. Szeto TH, Rowland SL, Habrukowich CL, King GF. 2003. The MinD membrane
734 targeting sequence is a transplantable lipid-binding helix. J Biol Chem 278:40050-6.
735 36. Karoui ME, Errington J. 2001. Isolation and characterization of topological specificity
736 mutants of minD in Bacillus subtilis. Mol Microbiol 42:1211-21.
737 37. Hayashi I, Oyama T, Morikawa K. 2001. Structural and functional studies of MinD
738 ATPase: implications for the molecular recognition of the bacterial cell division
739 apparatus. EMBO J 20:1819-28.

740 38. Wu W, Park KT, Holyoak T, Lutkenhaus J. 2011. Determination of the structure of the
741 MinD-ATP complex reveals the orientation of MinD on the membrane and the
742 relative location of the binding sites for MinE and MinC. Mol Microbiol 79:1515-28.
743 39. Story RM, Steitz TA. 1992. Structure of the recA protein-ADP complex. Nature
744 355:374-6.
745 40. Leonard TA, Butler PJ, Lowe J. 2005. Bacterial chromosome segregation: structure
746 and DNA binding of the Soj dimer - a conserved biological switch. Embo J.
747 41. Landgraf D, Okumus B, Chien P, Baker TA, Paulsson J. 2012. Segregation of molecules
748 at cell division reveals native protein localization. Nat Methods 9:480-2.
749 42. Lewis PJ, Marston AL. 1999. GFP vectors for controlled expression and dual labelling
750 of protein fusions in *Bacillus subtilis*. Gene 227:101-10.
751 43. Ghosal D, Trambaiolo D, Amos LA, Lowe J. 2014. MinCD cell division proteins form
752 alternating copolymeric cytomotive filaments. Nat Commun 5:5341.
753 44. Conti J, Viola MG, Camberg JL. 2015. The bacterial cell division regulators MinD and
754 MinC form polymers in the presence of nucleotide. FEBS Lett 589:201-6.
755 45. Huang H, Wang P, Bian L, Osawa M, Erickson HP, Chen Y. 2018. The cell division
756 protein MinD from *Pseudomonas aeruginosa* dominates the assembly of the MinC-
757 MinD copolymers. J Biol Chem 293:7786-7795.
758 46. Wang N, Zhang T, Du S, Zhou Y, Chen Y. 2022. How Do MinC-D Copolymers Act on Z-
759 Ring Localization Regulation? A New Model of *Bacillus subtilis* Min System. Front
760 Microbiol 13:841171.
761 47. Park KT, Du S, Lutkenhaus J. 2015. MinC/MinD copolymers are not required for Min
762 function. Mol Microbiol 98:895-909.
763 48. Strahl H, Hamoen LW. 2010. Membrane potential is important for bacterial cell
764 division. Proc Natl Acad Sci USA 107:12281-6.
765 49. Gouttenoire J, Montserret R, Kennel A, Penin F, Moradpour D. 2009. An amphipathic
766 alpha-helix at the C terminus of hepatitis C virus nonstructural protein 4B mediates
767 membrane association. J Virol 83:11378-84.
768 50. Adams DW, Wu LJ, Errington J. 2015. Nucleoid occlusion protein Noc recruits DNA to
769 the bacterial cell membrane. EMBO J 34:491-501.
770 51. Allen MP, Tildesley DJ. 1987. Computer simulations of liquids.
771 52. Binder K, Heermann DW. 2002. Monte Carlo Simulation in Statistical Physics: An
772 Introduction, 4th ed, vol 80.
773 53. Whitelam S, Geissler PL. 2007. Avoiding unphysical kinetic traps in Monte Carlo
774 simulations of strongly attractive particles. J Chem Phys 127:154101.
775 54. Sanz E, Marenduzzo D. 2010. Dynamic Monte Carlo versus Brownian dynamics: A
776 comparison for self-diffusion and crystallization in colloidal fluids. J Chem Phys
777 132:194102.
778 55. Mika JT, Thompson AJ, Dent MR, Brooks NJ, Michiels J, Hofkens J, Kuimova MK. 2016.
779 Measuring the Viscosity of the *Escherichia coli* Plasma Membrane Using Molecular
780 Rotors. Biophys J 111:1528-1540.
781 56. Mullineaux CW, Nenninger A, Ray N, Robinson C. 2006. Diffusion of green
782 fluorescent protein in three cell environments in *Escherichia coli*. J Bacteriol
783 188:3442-8.
784 57. Ptacin JL, Lee SF, Garner EC, Toro E, Eckart M, Comolli LR, Moerner WE, Shapiro L.
785 2010. A spindle-like apparatus guides bacterial chromosome segregation. Nat Cell
786 Biol 12:791-8.

787 58. Leipe DD, Wolf YI, Koonin EV, Aravind L. 2002. Classification and evolution of P-loop
788 GTPases and related ATPases. J Mol Biol 317:41-72.
789 59. Surovtsev IV, Lim HC, Jacobs-Wagner C. 2016. The Slow Mobility of the ParA
790 Partitioning Protein Underlies Its Steady-State Patterning in Caulobacter. Biophys J
791 110:2790-2799.
792 60. MacCready JS, Hakim P, Young EJ, Hu L, Liu J, Osteryoung KW, Vecchiarelli AG, Ducat
793 DC. 2018. Protein gradients on the nucleoid position the carbon-fixing organelles of
794 cyanobacteria. Elife 7.
795 61. Veiga H, Jousselin A, Schaper S, Saraiva BM, Marques LB, Reed P, Wilton J, Pereira
796 PM, Filipe SR, Pinho MG. 2023. Cell division protein FtsK coordinates bacterial
797 chromosome segregation and daughter cell separation in *Staphylococcus aureus*.
798 EMBO J doi:10.15252/embj.2022112140:e112140.
799 62. Deeng J, Chan KY, van der Sluis EO, Berninghausen O, Han W, Gumbart J, Schulten K,
800 Beatrix B, Beckmann R. 2016. Dynamic Behavior of Trigger Factor on the Ribosome. J
801 Mol Biol 428:3588-602.
802 63. Ishikawa K, Matsuoka S, Hara H, Matsumoto K. 2017. Septal membrane localization
803 by C-terminal amphipathic alpha-helices of MinD in *Bacillus subtilis* mutant cells
804 lacking MinJ or DivIVA. Genes Genet Syst 92:81-98.
805 64. Suefuji K, Valluzzi R, RayChaudhuri D. 2002. Dynamic assembly of MinD into filament
806 bundles modulated by ATP, phospholipids, and MinE. Proc Natl Acad Sci U S A
807 99:16776-81.
808 65. Hamoen LW, Smits WK, de Jong A, Holsappel S, Kuipers OP. 2002. Improving the
809 predictive value of the competence transcription factor (ComK) binding site in
810 *Bacillus subtilis* using a genomic approach. Nucleic Acids Res 30:5517-28.
811 66. Morimoto T, Loh PC, Hirai T, Asai K, Kobayashi K, Moriya S, Ogasawara N. 2002. Six
812 GTP-binding proteins of the Era/Obg family are essential for cell growth in *Bacillus*
813 *subtilis*. Microbiology 148:3539-52.
814 67. Fort P, Errington J. 1985. Nucleotide sequence and complementation analysis of a
815 polycistronic sporulation operon, *spoVA*, in *Bacillus subtilis*. J Gen Microbiol
816 131:1091-105.
817 68. Syvertsson S, Wang B, Staal J, Gao Y, Kort R, Hamoen LW. 2021. Different Resource
818 Allocation in a *Bacillus subtilis* Population Displaying Bimodal Motility. J Bacteriol
819 203:e0003721.
820 69. Vischer NO, Verheul J, Postma M, van den Berg van Saparoea B, Galli E, Natale P,
821 Gerdes K, Luirink J, Vollmer W, Vicente M, den Blaauwen T. 2015. Cell age dependent
822 concentration of *Escherichia coli* divisome proteins analyzed with ImageJ and
823 ObjectJ. Front Microbiol 6:586.
824
825

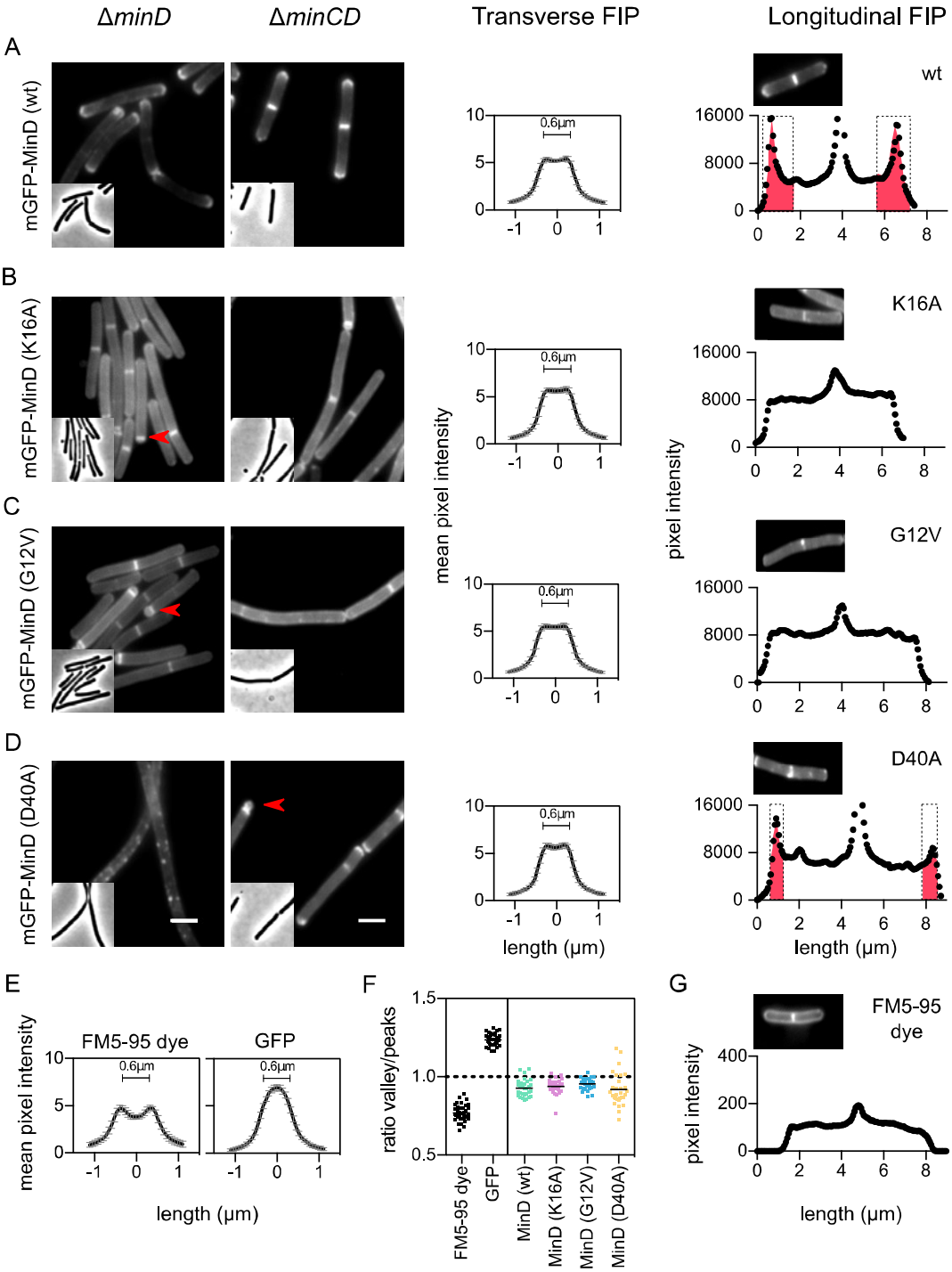

Fig. 1. Localization of monomeric and dimeric MinD variants

Cellular localization of (A) wild type MinD, (B) MinD K16A (apo monomer), (C) MinD G12V (ATP-bound monomer), and (D) MinD D40A (ATP-bound dimer, ATP hydrolysis deficient). Localization was monitored by an N-terminal mGFP fusion. Fusion proteins were expressed at the ectopic *amyE* locus, under control of a xylose-inducible promoter in either a Δ*minD* or

832 Δ*minCD* background. Fluorescence images (left panels) and corresponding phase contrast
833 images (inset) are shown in the left panels. Some minicells are indicated with red arrows.
834 Scale bar is 2 µm. Middle panels show the transverse fluorescence intensity profiles (FIP)
835 calculated using an average of at least 30 cells (Δ*minCD* background) per data set. Right
836 panels depict the longitudinal fluorescence intensity profiles (FIP) using the Δ*minCD*
837 background. The manually shaded red areas highlight the polar gradients. Additional
838 examples for wild type MinD and the D40A variants are shown in Fig. S3. (E) Transversal
839 fluorescence intensity profile (FIP) of exponentially growing wild-type cells stained with
840 fluorescence membrane dye FM5-95, and wild-type cells expressing GFP are shown as
841 controls. (F) Membrane affinities estimated from the valley/peak ratios shown in the middle
842 panels of (A-D) and controls (E). (G) Longitudinal fluorescence intensity profile (FIP) along
843 the exponentially growing wild-type cells stained with the fluorescence membrane dye
844 FM5-95. Strains used in (A): LB249 and LB305, (B): LB250 and LB306, (C): LB251 and LB307,
845 (D): LB252 and LB308, (E): LB609 and (G) 168.

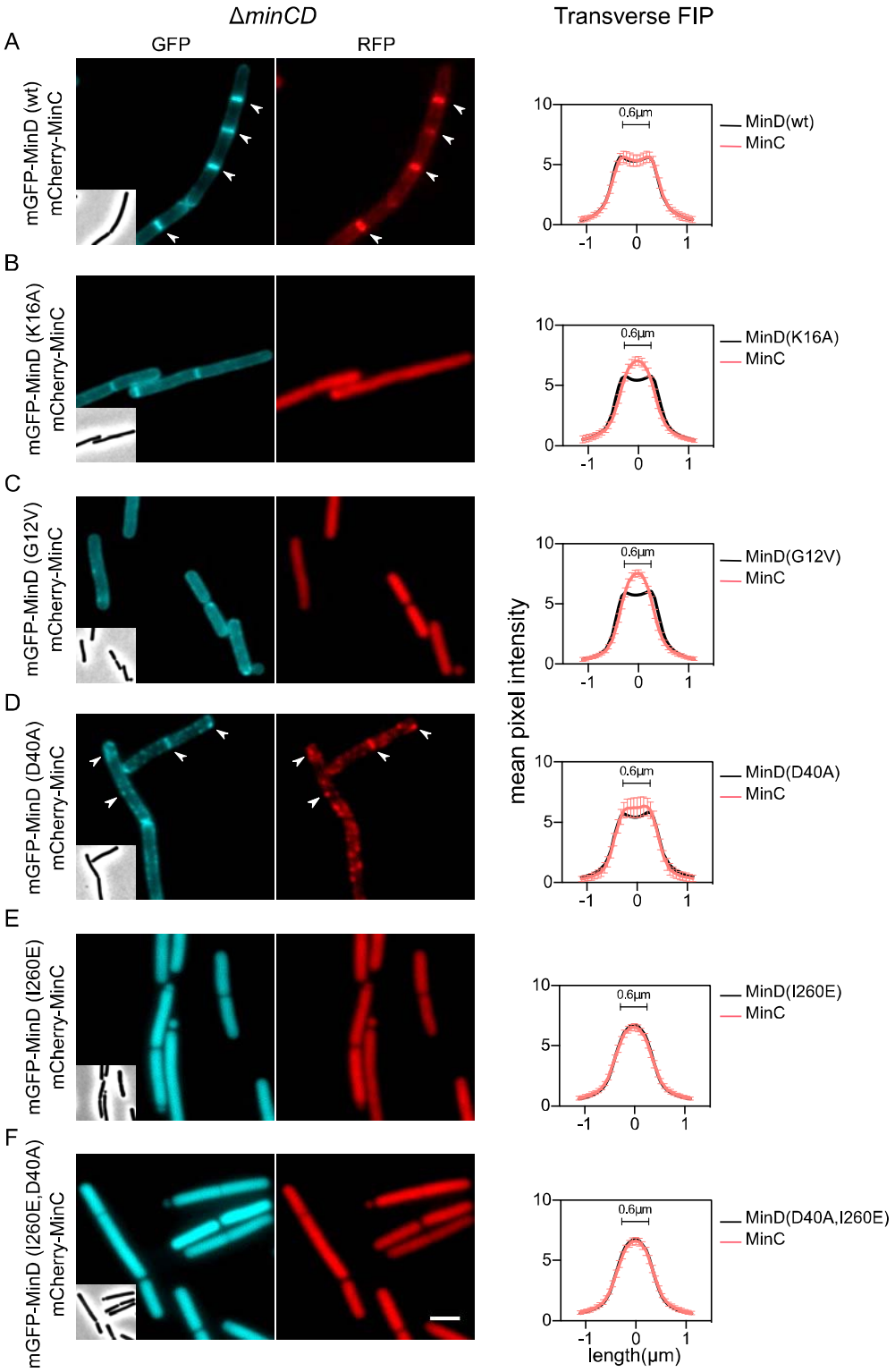

Fig. 2. Membrane recruitment of MinC by MinD variants

Fluorescence microscopy images of cells expressing different mGFP–MinD variants (cyan) and mCherry–MinC (red). Corresponding phase contrast images shown in the insets. (A)

850 Wild type MinD, (B) MinD K16A (apo monomer), (C) MinD G12V (ATP-bound monomer), (D)
851 MinD D40A (ATP-bound fixed dimer), (E) MinD I260E (non-membrane binding), (F) MinD
852 D40A, I260E (non-membrane binding ATP-bound fixed dimer). Right panels show the
853 transverse fluorescence intensity profiles (FIP) averaged over at least 30 cells. White arrows
854 in (D) highlights colocalization. Scale bar is 2 µm. mGFP–MinD variants were expressed in a
855 Δ*minCD* background strain from the ectopic *amyE* locus under a xylose-inducible promoter
856 (0.1 % xylose), and mCherry–MinC was expressed from the ectopic *aprE* locus under an
857 IPTG-inducible promoter (0.01 mM IPTG). Strains used: (A) LB318, (B) LB319, (C) LB320, (D)
858 LB321. (E) LB643 and (F) LB644.

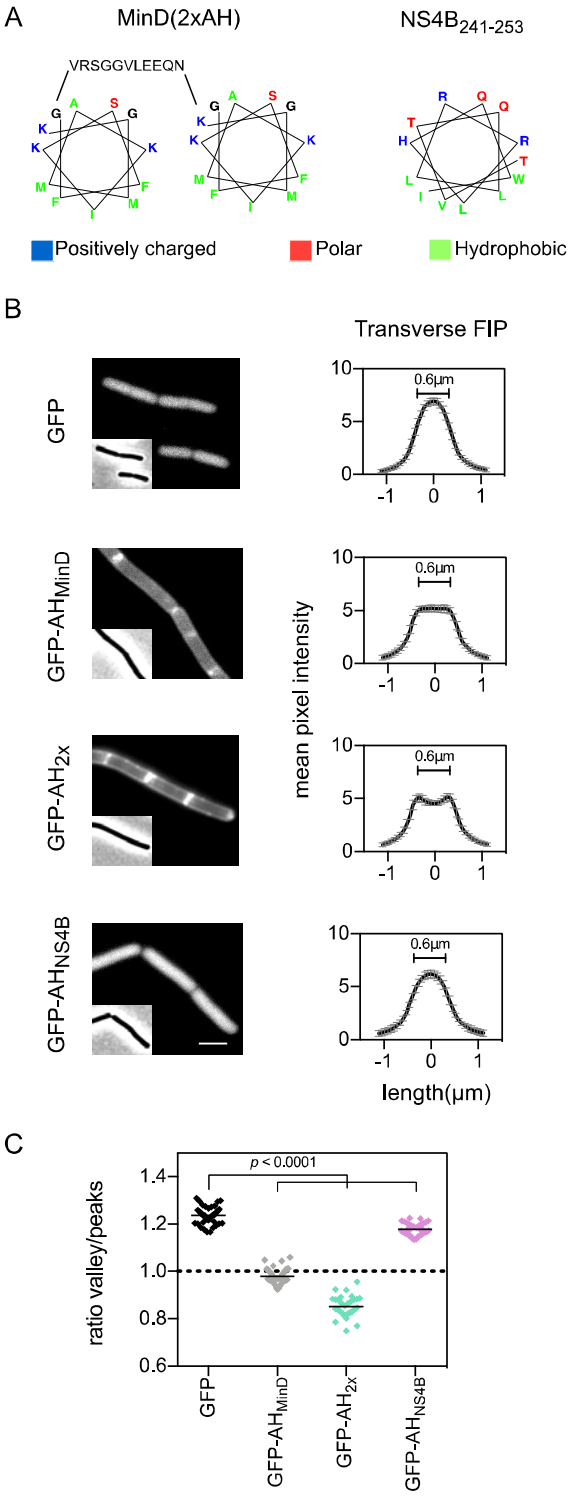

Fig. 3. Membrane association of different amphipathic helices

(A) Schematic presentation of the tandem amphipathic helix and the weak amphipathic helix from Hepatitis C virus protein $NS4B_{241\text{-}253}$. (B) Fluorescence microscopy images and transverse fluorescence intensity profiles of cells expressing the different amphipathic helix

864 sequences fused to the C-terminus of GFP. A strain expressing cytoplasmic GFP was included
865 for comparison. Scale bar is 2 µm. Strains used: FBB043 (GFP-AH_{MinD}), FBB05 (GFP-AH_{2x}),
866 FBB046 (GFP-AH_{NS4B}), LB609 (GFP). (C) Average membrane affinities calculated from the
867 transverse fluorescence intensity profiles ($n > 30$).

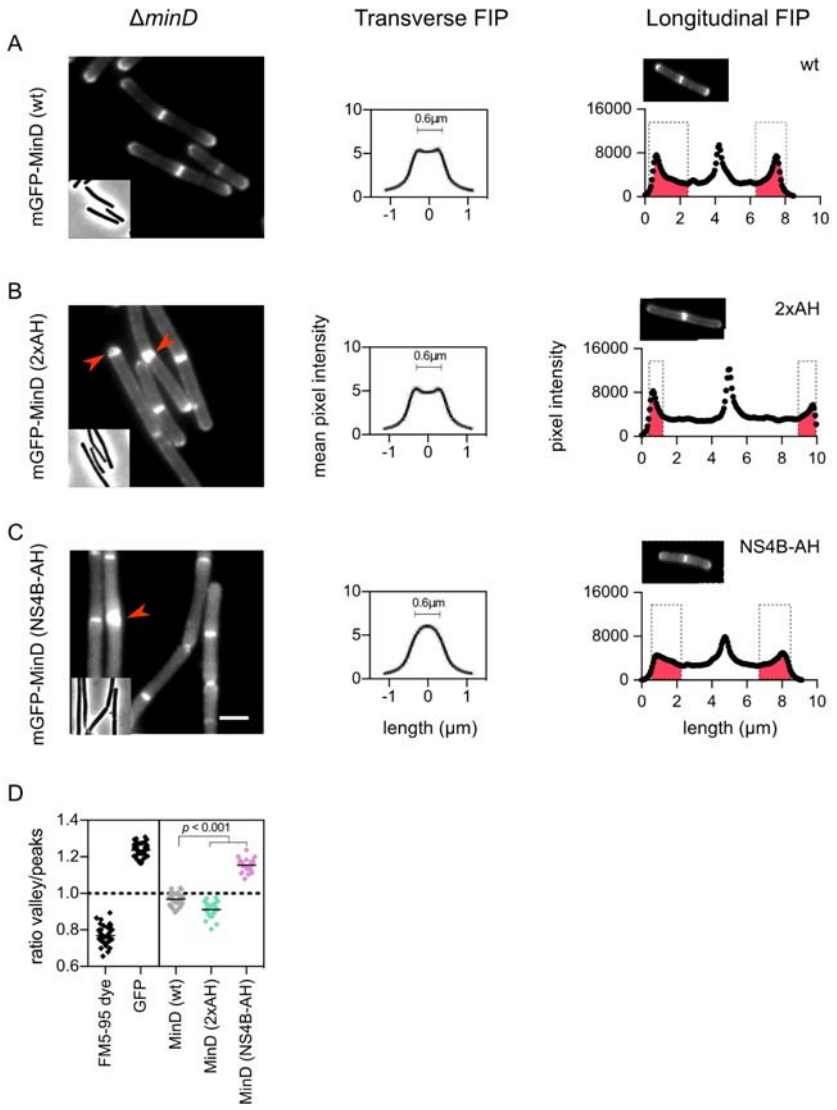

868

869 **Fig. 4. Membrane affinity affects MinD gradient**

870 Fluorescence microscopy and fluorescence intensity profiles (right panels) of cells
871 expressing mGFP-MinD containing either the native amphipathic helix (wt) (A), the tandem
872 MinD amphipathic helix (2xAH) (B) or the weak Hepatitis C virus protein NS4B amphipathic
873 helix (NS4B-AH) (C). The manually shaded red areas highlight the polar gradients. Additional
874 examples are shown in Fig. S5. (D) Relative membrane affinities of the different mGFP-MinD
875 variants calculated from transverse fluorescence intensity profiles (n > 30). The MinD
876 variants were expressed in a Δ*minD* background from the ectopic *amyE* locus under control
877 of a xylose-inducible promoter (0.1 % xylose). Phase contrast images are shown as insets.
878 Some double septa are indicated with red arrows. Scale bar is 2 µm. Red areas in the
879 intensity profiles highlight the polar gradients. Strains used in (A) LB249, in (B) LB507, in (C)

880 LB508.

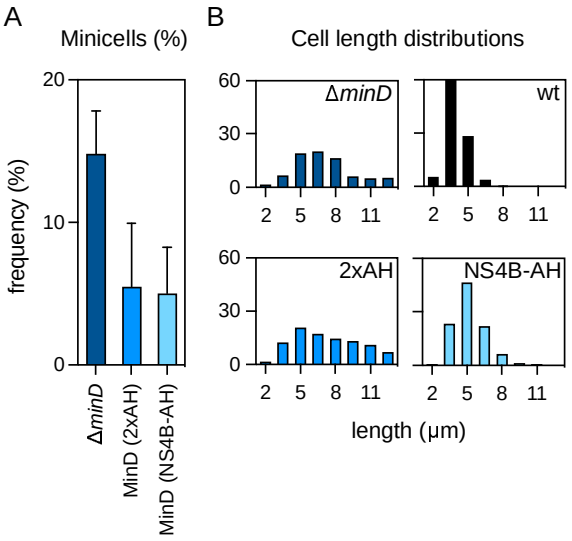

881

882 **Fig. 5. Functionality of MinD with different membrane affinities**

883 (A) Minicell formation in cells expressing mGFP-MinD with different membrane affinities.
884 The MinD variants were expressed in a Δ*minD* background from the ectopic *amyE* locus
885 under regulation of a xylose-inducible promoter (*n* > 300). (B) Cell length distributions of the
886 different strains (*n* > 300). Strains used: 1901 (Δ*minD*), LB249 (wild type MinD), LB507
887 (2xAH) and LB508 (NS4B-AH).

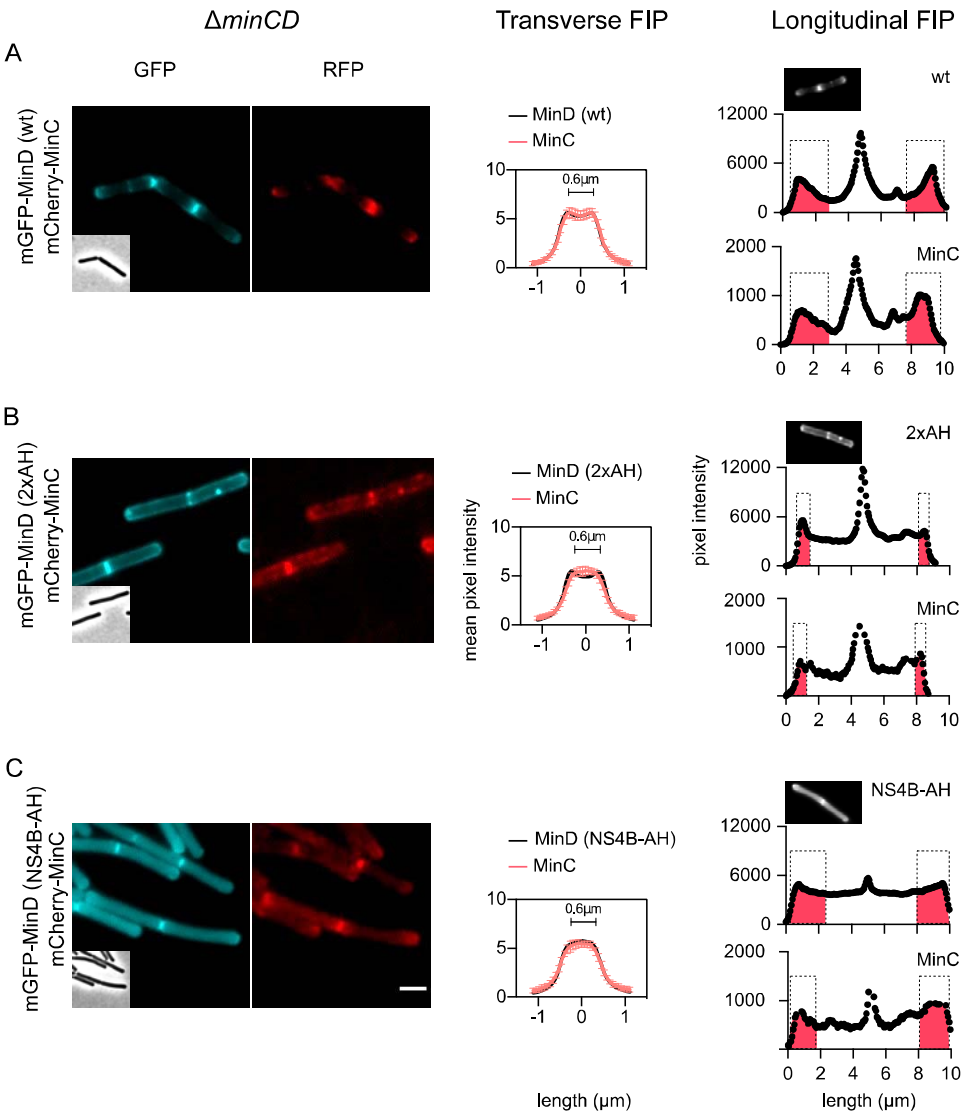

Fig. 6. Increased MinD membrane affinity affects MinC recruitment

Fluorescence microscopy images of cells expressing mGFP-MinD (cyan) and mCherry-MinC (red), with either the native membrane anchor (A), the tandem amphipathic helix (B), or the weak Hepatitis C virus protein NS4B derived amphipathic helix (C). Corresponding phase contrast images are shown in insets. Scale bar is 2 µm. Transverse fluorescence intensity profiles are shown in the right panels (n > 30). Right panels depict the longitudinal fluorescence intensity profiles (FIP) with manually shaded red areas to highlight the polar gradients. Additional examples are shown in Fig. S7. The mGFP-MinD variants were expressed at the ectopic *amyE* locus from a xylose-inducible promoter (0.1 % xylose), and mCherry-MinC was expressed at the ectopic *aprE* locus regulated by an IPTG-inducible promoter (0.01 mM IPTG) in a Δ*minCD* background strain. Strains used: (A) LB318, (B)

900 LB584, (C) LB559.

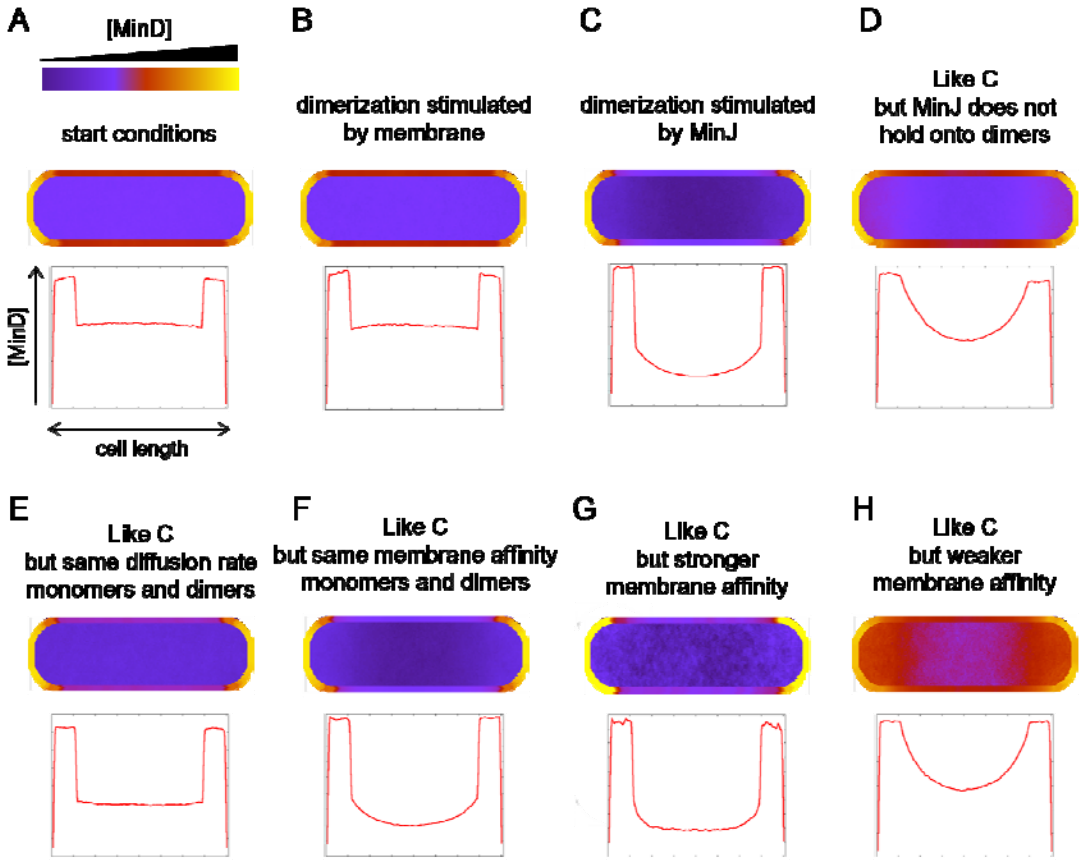

Fig. 7. Kinetic Monte Carlo simulations of MinD localization

Whole-cell kinetic Monte-Carlo simulations employing the following conditions. (A) Start situation whereby (i) diffusion along the membrane is 10-fold slower compared to cytoplasm, (ii) MinD dimer diffuses 2-fold slower compared to the monomer in both environments, (iii) 10 % stronger membrane affinity for dimer, (iv) membrane dwell time of monomers and dimers on average 1.4-4.5 sec, (v) dimerization and monomerization rates such that dimers and monomers are approximately in a 1:1 ratio, (vi) transition from dimer to monomer occurs stochastically with a half-life of approximately 1/sec, and (vii) MinD dimers in close proximity of polar regions (peak MinJ concentration) will remain attached for some time, so that approximately 25 % of MinD dimers is associated with the polar caps, representing MinJ. (B) Same as simulation A but membrane attached monomers have a 2-fold higher chance of forming dimers compared to cytoplasmic monomers. (C) Same as simulation A but MinJ also stimulates MinD dimerization. (D) Same as simulation C but MinD dimers are not retained by MinJ. (E) Same as simulation C but diffusion rates of monomer

918 and dimer are the same. (F) Same as simulation C but the membrane affinity of MinD
919 monomers and dimers is the same. (G) Same as simulation C but membrane affinity of MinD
920 is stronger (such that the diffusion is a further 10-fold slower on the membrane). (H) Same
921 as simulation C but membrane affinity of MinD is 2-fold weaker. Graphs indicate the average
922 lateral projection of MinD in simulated cells.
923